Supersaturation and particle dynamics in evaporating vertical falling films

Denis Vleeschhouwers

Department of Mechanics and Maritime Sciences Chalmers University of Technology Gothenburg, Sweden, 2025

Supersaturation and particle dynamics in evaporating vertical falling films

Denis Vleeschhouwers

Acknowledgments, dedications, and similar personal statements in this thesis, reflect the author's own views.

 $\ensuremath{\mathbb{C}}$ Denis Vleeschhouwers 2025 except where otherwise stated.

Department of Mechanics and Maritime Sciences Chalmers University of Technology SE-412 96 Gothenburg, Sweden Phone: +46 (0)31 772 1000

Printed by Chalmers Digital Printing Gothenburg, Sweden, November 2025

Supersaturation and particle dynamics in evaporating vertical falling films

Denis Vleeschhouwers Department of Mechanics and Maritime Sciences Chalmers University of Technology

Abstract

Crystallization fouling in industrial heat exchangers occurs when dissolved salt species in liquids exceed their solubility limits, leading to supersaturation, nucleation, and subsequent crystal deposition on heat-transfer surfaces. The resulting solid fouling layer increases thermal resistance and reduces system efficiency. This study aims to investigate the onset, evolution, and dynamics of supersaturation — the precursor of crystallization fouling — in vertical falling films to elucidate the coupled transport phenomena governed by film hydrodynamics. A two-phase Direct Numerical Simulation (DNS) framework based on the Volume of Fluid (VOF) method was developed to fully resolve hydrodynamics, heat transfer, and sufficiently capture the very fine scales of mass transport. The simulations show that supersaturation originates at the gas-liquid interface due to interfacial evaporation, while advection and diffusion redistribute it within the film through recirculation zones and local turbulence. The supersaturation dynamics exhibit a pronounced dependence on the Reynolds number (representing the wetting rate of the film), highlighting the strong coupling between the studied transport mechanisms. In parallel, as an ongoing work, a Lagrangian particle-tracking (LPT) framework was developed to investigate the transport of nucleated crystal seeds arising from supersaturated regions. The framework incorporates all relevant hydrodynamic forces, including near-wall corrections to drag and lift. Preliminary results indicate that shear-induced lift governs lateral particle migration toward the wall — a key mechanism for studying particle deposition. This coupled approach links supersaturation and particle transport, providing a foundation for predicting and mitigating crystallization fouling in industrial falling films.

Keywords: Supersaturation, Falling films, Evaporation, Volume of fluid, Lagrangian particle tracking

"Das Wichtigste ist, dass man nicht aufhört zu fragen."

List of Publications

This thesis is based on the following publications:

- [A] **Denis Vleeschhouwers**, Niklas Hidman, Anders Åkesjö, Henrik Ström, Srdjan Sasic, "Liquid supersaturation in evaporating vertical falling films A direct numerical simulation study". *International Journal of Heat and Mass Transfer*, vol. 255, pp. 127760 (2026).
- [B] **Denis Vleeschhouwers**, Niklas Hidman, Anders Åkesjö, Henrik Ström, Srdjan Sasic, "Inertial particle dynamics in vertical wavy falling films". *To be submitted to a scientific journal* (2026).

Contents

ΑI	ostra	et	i
Li	st of	Papers	v
Αd	cknov	/ledgements i	x
Αd	crony	ms i	x
ı	Ex	tended Summary	1
1	Intr	oduction	3
	1.1	Falling film evaporators	3
	1.2		4
	1.3		6
2	Met	hodology	7
	2.1	Eulerian modeling approach	9
	2.2	Lagrangian particle tracking approach	1
3	Sele	ected challenges 1	3
	3.1	Numerical method for passive scalar advection	3

	3.2 Scalar diffusion from interfacial cells	17
4	Concluding Remarks and Future Work	27
Re	eferences	29
H	Papers	33
Α	Liquid supersaturation in evaporating vertical falling films - A direct numerical simulation study	Α1
В	Inertial particle dynamics in vertical wavy falling films	В1

Acknowledgments

I would like to express my gratitude to my main supervisor, Srdjan Sasic, for the opportunity to pursue a PhD in fluid mechanics and for his continuous guidance throughout the project. I have greatly valued our discussions, which often challenged my views and strengthened the quality of our research. My deepest thanks also to my co-supervisor, Niklas Hidman. I could not imagine a better mentor at my current academic stage when it comes to discussing fluid mechanics, physics, and numerical methods. I am grateful for the opportunity to continue learning from you. I would like to thank my examiner, Henrik Ström, for his valuable guidance and constructive feedback, and Anders Åkesjö for sharing important industrial perspectives. To my colleagues at the Division of Fluid Dynamics, it has been a pleasure to get to know you and your work. A special thanks to the multiphase group for the friendships that made this journey especially rewarding. Finally, I would like to extend my warmest and deepest gratitude to my family back in Germany, friends and to Ellen for your encouragement, love, and support.

Collaboration with, and the financial support of, the Resourcesmart Processes Network financed by Vinnova via BioInnovation (2021-02078) and industrial partners (Billerud, SCA, Stora Enso, Södra Skogsägarna, Valmet, and RISE) is gratefully acknowledged. The computations were enabled by resources provided by the National Academic Infrastructure for Supercomputing in Sweden (NAISS), partially funded by the Swedish Research Council through grant agreement no. 2022-06725.

Acronyms

DNS: Direct Numerical Simulation

LPT: Lagrangian Particle Tracking

PLIC: Piecewise Linear Interface Calculation

VOF: Volume Of Fluid

Part I Extended Summary

CHAPTER 1

Introduction

The global transition towards a sustainable society necessitates a significant reduction in carbon emissions and a shift from fossil fuels to renewable energy sources. Despite growing awareness of environmental challenges, modern society remains heavily dependent on fossil-based energy systems. Given the continual rise in global population and living standards, the overall energy demand is expected to increase rather than decline in the foreseeable future. Achieving sustainability, therefore, not only requires the adoption of renewable energy sources but also the efficient utilization and reuse of available energy within industrial and domestic systems.

1.1 Falling film evaporators

Improving energy efficiency is a crucial step toward achieving a sustainable society. One effective strategy is the recovery and reuse of waste heat, in which high-performance heat exchangers play a central role by enabling efficient heat transfer with minimal losses [1]. Among the various types, falling film units are particularly attractive due to their excellent thermal and mass transport characteristics. In these systems, a thin liquid film flows down an in-

clined or vertical surface with a distinct gas-liquid interface, allowing for high heat transfer performance even under small temperature differences. Owing to these advantages, falling film heat exchangers are widely applied in industrial processes such as condensers, heaters, and evaporators. Their ability to handle viscous and heat-sensitive fluids makes them suitable for applications requiring gentle thermal treatment [2]. In the food industry, for example, falling film evaporators are widely employed for concentrating heat-sensitive products such as fruit juices or dairy solutions, enabling the production of concentrated juices and dairy powders without compromising product quality. In the pulp and paper industry, these systems play a critical role in concentrating black liquor within the chemical recovery process, where the concentrated liquor is subsequently combusted to regenerate cooking chemicals and recover energy [3]. Beyond these applications, falling film heat exchangers are also extensively utilized in the chemical and petrochemical industries, wastewater treatment, and in pharmaceutical and biomedical processes, where efficient heat and mass transfer under gentle operating conditions is essential. Although falling film units offer high energy efficiency and operational flexibility, their performance can be severely constrained by several industrial challenges, among which crystallization fouling is among the most significant [1], [3].

1.2 Crystallization fouling

Crystallization fouling constitutes a critical operational issue in numerous industrial processes, including but not limited to evaporating falling liquid films. It involves the formation and deposition of crystalline solids, immersed in the industrial fluid of interest, on heat transfer surfaces, which introduces an additional thermal resistance layer, thereby degrading heat transfer performance and increasing pressure losses within the system. Over time, these deposits reduce process efficiency, necessitate frequent maintenance, and can cause unscheduled shutdowns — culminating in substantial economic and energy penalties in continuous industrial operations [4].

From a fundamental perspective, crystallization fouling proceeds through a sequence of interrelated stages: **supersaturation**, **crystal nucleation**, **crystal growth**, **crystal transport**, and **deposition** (or **detachment**) at the heat transfer surface, compare Fig. (1.1). Supersaturation represents the essential thermodynamic driving force, governing both the onset of nucleation

and the subsequent growth of crystalline structures in the specific regions of supersaturation. It arises when the solute concentration exceeds its equilibrium solubility, producing a metastable solution capable of undergoing a phase transition from dissolved species to solid crystals [5]. According to classical nucleation theory, spontaneous formation of stable nuclei occurs once a critical supersaturation threshold is surpassed [6].

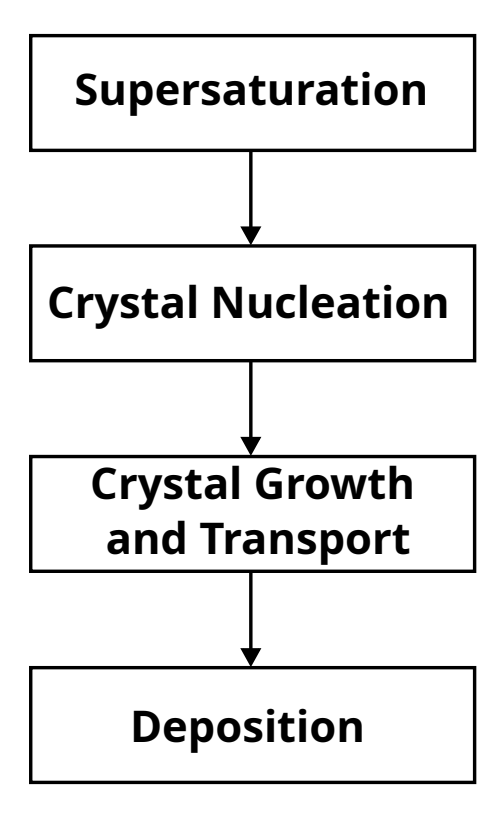


Figure 1.1: Schematic representation of the general sequential processes leading to the onset and development of crystallization fouling, exemplified here for evaporating falling liquid films.

In evaporating falling liquid films, the mechanisms responsible for the generation of supersaturation are only partially understood. This study hypothesizes that supersaturation develops primarily through two concurrent phe-

nomena: inverse solubility of the solute — where solubility decreases with increasing temperature (i.e., in the vicinity of the heated wall) [7] — and solvent evaporation at the gas-liquid interface, which locally elevates the solute concentration. Although each mechanism could independently promote supersaturation, their coupled effects and relative contributions have not been comprehensively quantified. A detailed understanding of these interacting processes is essential for elucidating the onset of crystallization fouling and for developing predictive models and mitigation strategies aimed at sustaining heat exchanger performance and extending operational reliability.

1.3 Thesis outline

This thesis begins with an introduction to the concept of evaporating falling liquid films, outlining the fundamental physical mechanisms and highlighting their relevance across a wide range of industrial applications. The discussion then turns to the adverse effects of crystallization fouling in these systems, followed by the formulation of a hypothesis describing how such flows can develop regions of supersaturation — the precursor to the crystallization fouling phenomenon — under the prevailing physical conditions of the system.

Chapter 2 presents the numerical framework developed to investigate the onset and dynamics of supersaturation regions, including the integration of Lagrangian particle tracking into the model. Chapter 3 focuses on the principal numerical challenges encountered during the development of the Eulerian framework and its application to accurately analyze and study liquid supersaturation fields in evaporating falling films. The main emphasis of this introductory part lies on this section for two reasons: i) to emphasize the importance of addressing these challenges during the framework development, and ii) to provide a more comprehensive discussion than that included in the appended papers.

Finally, Chapter 4 briefly summarizes the main findings and outlines prospective directions for future research in the continued development of this work. For a detailed presentation of the obtained results, together with a corresponding discussion, the reader should consult the appended papers.

CHAPTER 2

Methodology

We investigate the onset and transport dynamics of liquid-phase supersaturation in evaporating vertical falling films on smooth heat transfer surfaces. To capture the coupled behavior of film hydrodynamics, heat transfer, and mass transfer, a comprehensive numerical framework is developed. Evaporation at the gas—liquid interface enriches the solute concentration locally, while the presence of inversely soluble salt species within the film can induce the formation of supersaturated regions at high temperature locations, compare our hypothesis in 1.2 and [8]. Supersaturation is mathematically defined following [3] as

$$S(t, \mathbf{x}) = \frac{C_{salt}(t, \mathbf{x})}{C_{salt}^{sat}(T(t, \mathbf{x}))} \begin{cases} \text{Supersaturation} & \text{if } S(t, \mathbf{x}) > 1\\ \text{Undersaturation/Saturation} & \text{if } S(t, \mathbf{x}) \leq 1. \end{cases}$$
(2.1)

where $S(t, \mathbf{x})$ denotes the local level of supersaturation at time t and position $\mathbf{x} = (x, y)$ in the film. Undersaturation, saturation, and supersaturation correspond respectively to $S(t, \mathbf{x}) < 1$, $S(t, \mathbf{x}) = 1$, and $S(t, \mathbf{x}) > 1$. The quantity $C_{salt}(t, \mathbf{x})$ represents the salt concentration, modeled as a passive scaler within the liquid phase, while $C_{salt}^{sat}(T(t, \mathbf{x}))$ is the temperature-dependent saturation concentration for the salt of interest. For salts exhibiting inverse solubility,

an increase in temperature $T(t, \mathbf{x})$ decreases $C_{salt}^{sat}(T(t, \mathbf{x}))$, thereby reducing solubility. Consequently, elevated temperatures near the heat transfer surface may drive the solution toward supersaturation. Simultaneously, evaporation at the gas-liquid interface removes solvent, increases the local salt concentration $C_{salt}(t, \mathbf{x})$ and enhancing the risk of supersaturation within these film regions. Importantly, the developed numerical framework is not restricted to a specific salt or solvent solution. By prescribing $C_{salt}^{sat}(t, \mathbf{x})$ appropriately, supersaturation behavior can be simulated for any industrial fluid of interest. To summarize this, the model problem, highlighting the gas-liquid interface and its interplay with temperature and concentration scalar fields, is illustrated in Fig. (2.1).

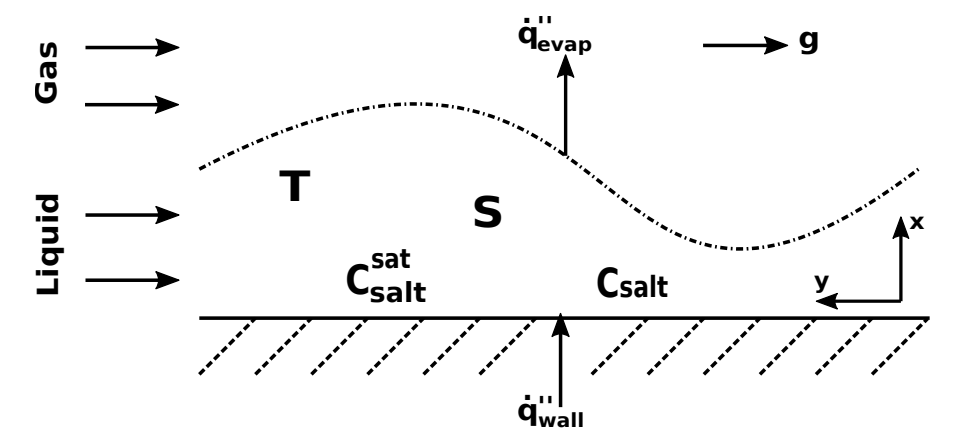


Figure 2.1: Wavy vertical falling liquid film with a gas-liquid interface illustrating the scalar fields relevant to the investigation of supersaturation onset and dynamics. Shown are the local temperature T, salt concentration C_{salt} , saturation concentration C_{salt}^{sat} , and supersaturation S, together with the wall and gas-liquid interface heat flux components. The figure is rotated 90° counterclockwise for clarity.

Following the investigation of liquid-phase supersaturation dynamics in vertical falling films, the formation of solid salt crystals in supersaturated regions (mitigation of the crystal nucleation process, see Fig. (1.1)) is modeled through the introduction of Lagrangian particles within the liquid film. This Eulerian–Lagrangian framework enables explicit tracking of individual particle trajectories, allowing for the analysis of how local film hydrodynamics and

particle size influence particle motion and transport behavior. By an attempt to couple supersaturation fields with the Lagrangian particle dynamics, the model aims at establishing a direct link between the onset of supersaturation and the subsequent evolution of solid-phase particles within the film. This approach facilitates a detailed examination of the particle transport mechanisms toward the heated wall, where deposition completes the crystallization fouling process at the solid boundary. A schematic representation of Lagrangian particles within a wavy falling film is shown in Fig. (2.2).

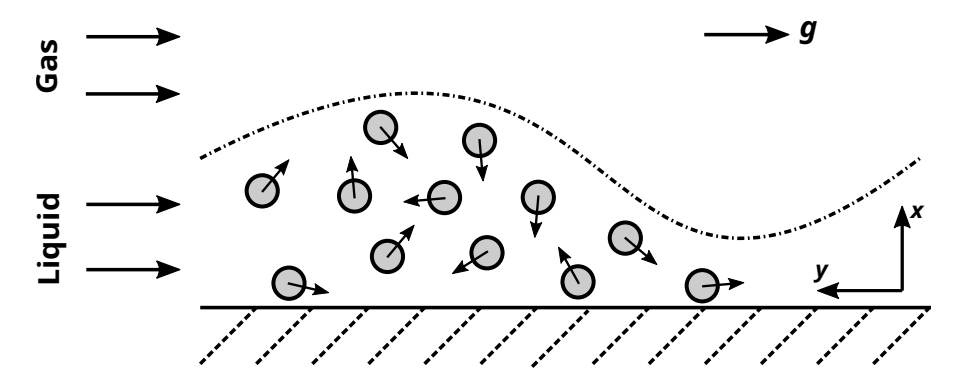


Figure 2.2: Wavy vertical falling liquid film with a well-defined gas—liquid interface (dashed line) containing rigid spherical particles suspended in the liquid phase. The film flows downward along the negative y-direction, with thickness measured in the positive x-direction; the bottom surface represents the solid wall. Arrows indicate the instantaneous particle motion (schematically). The figure is rotated 90° counterclockwise for clarity.

2.1 Eulerian modeling approach

Direct Numerical Simulations (DNS) are performed using a geometric Volume-of-Fluid (VOF) method to fully resolve the hydrodynamics and interfacial dynamics of the falling film, as well as the associated heat transfer and to sufficiently capture the small-scale structures of the thin mass transfer boundary layer. The governing equations are expressed in non-dimensional form (represented with Θ), employing the viscous length scale of the film, $(\nu_l^2/g)^{1/3}$,

as the characteristic length, where ν_l denotes the liquid kinematic viscosity and g the gravitational acceleration [9]. The incompressible two-phase Navier–Stokes equations, which describe the film dynamics, are coupled with the transport equations for the volume fraction f, temperature T^{Θ} , and salt concentration C^{Θ}_{solt} , as follows:

$$\nabla^{\Theta} \cdot \mathbf{u}^{\Theta} = 0, \tag{2.2}$$

$$\begin{split} \frac{\partial \mathbf{u}^{\Theta}}{\partial t^{\Theta}} + \nabla^{\Theta} \cdot (\mathbf{u}^{\Theta} \mathbf{u}^{\Theta}) &= -\frac{1}{\rho^{\Theta}} \nabla^{\Theta} p^{\Theta} + \nabla^{\Theta} \cdot \left[\nu^{\Theta} (\nabla^{\Theta} \mathbf{u}^{\Theta} + (\nabla^{\Theta} \mathbf{u}^{\Theta})^{T}) \right] \\ &+ \mathbf{g}^{\Theta} + Ka \delta^{\Theta} \kappa^{\Theta} \mathbf{n}, \end{split} \tag{2.3}$$

$$\frac{\partial f}{\partial t^{\Theta}} + \nabla^{\Theta} \cdot (\mathbf{u}^{\Theta} f) = 0, \tag{2.4}$$

$$\frac{\partial T^{\Theta}}{\partial t^{\Theta}} + \nabla^{\Theta} \cdot (\mathbf{u}^{\Theta} T^{\Theta}) = \nabla^{\Theta} \cdot \left(D_{thermal}^{\Theta} (\nabla^{\Theta} T^{\Theta}) \right) + S_{thermal}^{\Theta}, \tag{2.5}$$

$$\frac{\partial C_{salt}^{\Theta}}{\partial t^{\Theta}} + \nabla^{\Theta} \cdot (\mathbf{u}^{\Theta} C_{salt}^{\Theta}) = \nabla^{\Theta} \cdot (D_{mass}^{\Theta} (\nabla^{\Theta} C_{salt}^{\Theta})) + S_{mass}^{\Theta}. \tag{2.6}$$

Eq. (2.2) represents the continuity condition, while Eq. (2.3) describes the two-phase momentum balance in conservative form. Eq. (2.4) governs the evolution of the volume fraction field, and Eqs. (2.5) and (2.6) describe the transport of temperature and salt concentration, respectively. The equations employ non-dimensional variables: time t^{Θ} ; spatial coordinates \mathbf{x}^{Θ} (x^{Θ}, y^{Θ}) ; velocity $\mathbf{u}^{\Theta} = (u^{\Theta}, v^{\Theta})$; and the spatial gradient operator $\nabla^{\Theta} =$ $(\partial/\partial x^{\Theta}, \partial/\partial y^{\Theta})$. Additional quantities include gravitational acceleration $\mathbf{g}^{\Theta} =$ $(g_x^{\Theta}, g_y^{\Theta})$, density ρ^{Θ} , kinematic viscosity ν^{Θ} , pressure p^{Θ} , interface curvature κ^{Θ} , interface normal vector $\mathbf{n}=(n_x,n_y)$, and the Dirac delta distribution δ^{Θ} . The final term on the right-hand side of Eq. (2.3) contains the Kapitza number, defined as $Ka = \frac{\sigma}{\rho_1 \nu_1^{4/3} q^{1/3}}$, where σ denotes the surface tension. The Kapitza number characterizes the balance between surface tension and viscous-gravitational forces and, together with the curvature and normal vector terms, quantifies the additional acceleration induced by surface tension at the gas-liquid interface. Finally, Eqs. (2.5) and (2.6) incorporate the nondimensional thermal and mass diffusivities, $D^{\Theta}_{thermal}$ and D^{Θ}_{mass} , respectively,

as well as source terms, $S^{\Theta}_{thermal}$ and S^{Θ}_{mass} , to account for evaporation and salt enrichment effects.

The governing equations, Eqs. (2.2)–(2.6), are solved using the open-source, finite-volume-based code Basilisk [10], [11], [12]. Basilisk employs a quadtree-adaptive multigrid solver that efficiently resolves interfacial dynamics and has been extensively validated for multiphase DNS [13], [14], [15]. The numerical solution procedure, implementation and initial and boundary condition details are described thoroughly in $Paper\ A$ and [8].

2.2 Lagrangian particle tracking approach

The Eulerian numerical framework introduced and described in [8] and 2.1 is extended by a Lagrangian point-particle model. This Eulerian–Lagrangian approach enables the inclusion of solid spherical particles as a dispersed phase within the continuous liquid film. The motivation for this attempt arises naturally from the observation that in aqueous salt solutions flowing as vertical falling films and exposed to interfacial evaporation and inverse soluble salt species, regions exceeding the solubility limit lead to supersaturation and the nucleation of salt crystals (Fig. (1.1)). These crystals are subsequently transported by the local advective flow of the continuous phase and may deposit on solid boundaries, such as heat transfer surfaces in heat exchanger applications, thereby contributing to crystallization fouling.

To capture the transport and dynamics of these particles, their motion is described in a Lagrangian frame of reference. The velocity and position of each particle are determined by applying Newton's second law, which expresses the particle momentum balance as

$$m_p \frac{d\mathbf{u}_p}{dt} = \sum_{i=1} \mathbf{F}_i, \tag{2.7}$$

where m_p is the particle mass, \mathbf{u}_p the particle velocity vector $\mathbf{u}_p = (u_p, v_p)$, and \mathbf{F}_i represents the external forces acting on the particle. For the right-hand side of Eq.(2.7), the external forces contributing to particle acceleration are considered as

$$m_p \frac{d\mathbf{u}_p}{dt} = \mathbf{F}_G + \mathbf{F}_B + \mathbf{F}_{AM} + \mathbf{F}_D + \mathbf{F}_L, \qquad (2.8)$$

where \mathbf{F}_G and \mathbf{F}_B denote the gravitational and buoyancy forces, \mathbf{F}_{AM} the added-mass force, and \mathbf{F}_D and \mathbf{F}_L the drag and shear-induced lift forces, respectively. These forces are expressed as

$$\mathbf{F}_G = m_p \mathbf{g},\tag{2.9}$$

$$\mathbf{F}_B = -\rho_l V_p \mathbf{g},\tag{2.10}$$

$$\mathbf{F}_{AM} = \frac{1}{2} \rho_l V_p \left(\frac{D\mathbf{u}_l}{Dt} - \frac{d\mathbf{u}_p}{dt} \right), \tag{2.11}$$

$$\mathbf{F}_{D} = \frac{C_{D}}{2} \rho_{l} A_{p} \mid \mathbf{u}_{l} - \mathbf{u}_{p} \mid (\mathbf{u}_{l} - \mathbf{u}_{p}), \qquad (2.12)$$

$$\mathbf{F}_{L} = 1.61 d_{p}^{2} \sqrt{\rho_{l} \mu_{l}} \frac{(\mathbf{u}_{l} - \mathbf{u}_{p}) \times \omega_{l}}{\sqrt{|\omega_{l}|}}, \tag{2.13}$$

where $V_p = \frac{\pi}{6}d_p^3$ is the particle volume, $A_p = \frac{\pi}{4}d_p^2$ its projected area, \mathbf{u}_l the local liquid velocity, C_D the drag coefficient, and ω_l the vorticity vector of the liquid phase [16], [17]. In Eq. (2.11), the material derivative of the Lagrangian acceleration of the fluid is given by

$$\frac{D\mathbf{u}_l}{Dt} = \frac{\partial \mathbf{u}_l}{\partial t} + \mathbf{u}_l \cdot (\nabla \mathbf{u}_l), \qquad (2.14)$$

where the first term represents the Eulerian local (unsteady) acceleration and the second term the convective acceleration associated with spatial velocity gradients. The governing equation for particle transport, Eq.(2.8), together with the force contributions defined in Eqs. (2.9) - (2.13), is implemented in non-dimensional form within Basilisk and solved using a second-order accurate time-integration scheme. The procedure for non-dimensionalization, numerical implementation, and the specification of particle initial and boundary conditions, as well as the applied corrections to the drag and lift forces accounting for wall-bounded flow effects, are described in detail in $Paper\ B$.

CHAPTER 3

Selected challenges

In this section, we address the key challenges encountered during the development of the numerical framework used to investigate liquid supersaturation dynamics in evaporating vertical falling films. The discussion focuses primarily on the Eulerian formulation, as the extension with the Lagrangian particle framework remains an ongoing effort. Detailed results on the onset, evolution, and transport of supersaturated regions under varying hydrodynamic conditions are presented in $Paper\ A$ and [8]. The following subsections focus on key numerical aspects, starting with the advection of a passive scalar field confined to a single phase within a multiphase VOF framework, and continuing with the treatment of scalar diffusion from interfacial (gas—liquid) cells, for which a dedicated numerical approach has been developed.

3.1 Numerical method for passive scalar advection

As formulated in 2, supersaturation is investigated exclusively within the liquid phase of a falling film. Accordingly, the scalar field representing the salt concentration, C_{salt}^{Θ} , is defined only in the liquid phase, while $C_{salt}^{\Theta}=0$ in the gas-phase of the computational domain. In this configuration, the falling

film consists of an aqueous salt solution flowing downward along the vertical wall. At the initial time $t^{\Theta} = t^{\Theta}_{init} = 0$, the salt concentration is prescribed as $C^{\Theta}_{salt}(t^{\Theta}_{init}) = 0.43$, see [8]. This value serves merely as an initial condition and can be adjusted according to the application of interest. In the absence of phase change and diffusion, the transport of C^{Θ}_{salt} occurs solely through advection by the liquid velocity field \mathbf{u}^{Θ} . Consequently, the total salt mass within the liquid phase must remain conserved over time, implying that

$$\langle C_{salt}^{\Theta} \rangle (t_{init}^{\Theta}) = \langle C_{salt}^{\Theta} \rangle (t_{end}^{\Theta}) = 0.43,$$
 (3.1)

where the liquid averaged salt concentration $\langle C_{salt}^{\Theta} \rangle$ at t_{init}^{Θ} equals the liquid averaged salt concentration at the end time of the simulation t_{end}^{Θ} . Under these assumptions, the non-dimensional scalar transport equation (Eq. 2.6) simplifies to the purely advective form

$$\frac{\partial C_{salt}^{\Theta}}{\partial t^{\Theta}} + \nabla^{\Theta} \cdot (\mathbf{u}^{\Theta} C_{salt}^{\Theta}) = 0. \tag{3.2}$$

Fig. (3.1) illustrates the simultaneous advection of the liquid volume fraction field f (subfigure (a)) and the salt concentration field C_{salt}^{Θ} (subfigure (b)). The liquid volume fraction f evolves according to the pure advection equation defined in Eq. (2.4). Ideally, the salt concentration field C_{salt}^{Θ} should be strictly confined to the liquid phase and advected consistently with the motion of f, such that its transport precisely follows the liquid volume fraction and the gas-liquid interface. However, as evident from Figure (3.1)(b), the salt concentration is not conserved in the liquid phase: nonphysical leakage of C_{salt}^{Θ} through the gas-liquid interface and into the gas phase occurs. This discrepancy originates from the different numerical treatments used for the two fields. In Basilisk, the advection of the volume fraction field f is performed using the Piecewise Linear Interface Calculation (PLIC) method. In this numerical scheme, the gas-liquid interface within each computational cell is first geometrically reconstructed from the cell's volume fraction of the previous time step. In a subsequent step, the flux during one time step is geometrically calculated, based on the information from the reconstructed interface. This two step scheme ensure accurate flux calculation while the liquid volume is conserved to machine precision [18]. In contrast, the advection of the scalar field C_{salt}^{Θ} does not employ the same geometrically conservative flux computation, rather a standard second order upwind scheme. As a result, the scalar field is subject to spurious diffusion across the gas-liquid interface, leading

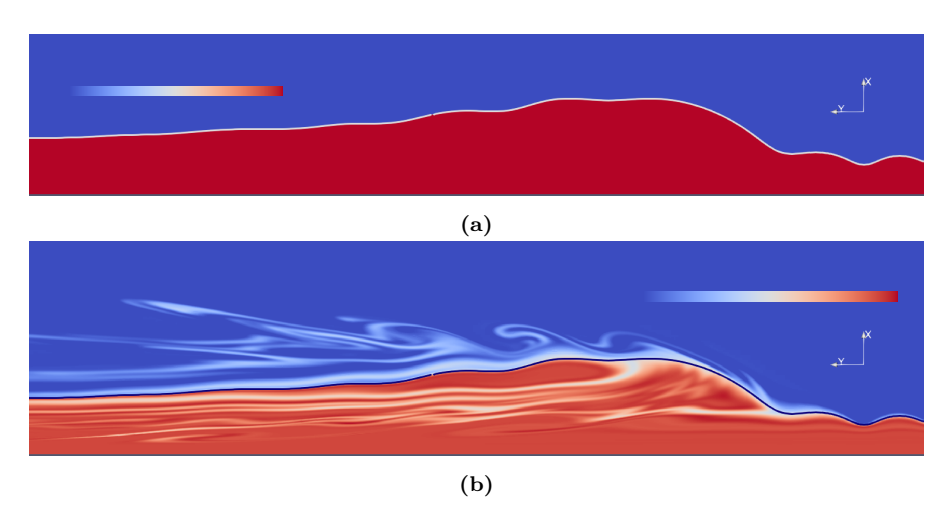


Figure 3.1: (a) Advection of the liquid volume fraction field f and (b) the salt concentration field C_{salt}^{Θ} . Flow conditions are defined by a Reynolds number Re=200 and a Kapitza number Ka=500. An initial concentration of $C_{salt}^{\Theta}(t_{init}^{\Theta})=0.43$ is prescribed in the liquid phase. The results show that C_{salt}^{Θ} does not follow the advection of f and diffuses into the gas phase, indicating violation of salt mass conservation in the liquid phase. Both subfigures are rotated 90° counterclockwise for clarity; the white line in (a) and the black line in (b) indicate the gasliquid interface.

to nonphysical transport of salt into the gas phase. This phenomenon, often referred to as $artificial\ mass\ diffusion$, is a purely numerical artifact that arises when a passive scalar is advected without consistent phase-restricted flux treatment, such as the numerical treatment for the advection of f.

To ensure physically consistent transport of the salt concentration field, it is therefore essential to apply the same geometric flux calculation scheme used for the volume fraction field f also to C_{salt}^{Θ} . Previous studies, such in [19] and [20], have detailed the derivation and description of geometric advection schemes for passive scalars in multiphase flows. Following a similar approach to this studies, the present framework employs the interface geometry reconstructed in the first step of the PLIC method to compute geometrical fluxes for both f and C_{salt}^{Θ} in a consistent and simultaneous manner. By using the same

geometrically defined interface during the second step of PLIC — the flux computation stage — the advection of the scalar and the liquid volume fraction are performed synchronously, ensuring strict phase confinement of C_{salt}^{Θ} and eliminating artificial diffusion across the gas-liquid interface.

The results of the improved advection scheme for the coupled transport of f and C_{salt}^{Θ} are presented in Figure (3.2). Subfigure (a) shows the liquid volume fraction field f, while subfigure (b) denotes the corresponding salt concentration field C_{salt}^{Θ} . In contrast to Figure (3.1) (b), it is evident that C_{salt}^{Θ} is now strictly confined to the liquid phase, with no nonphysical or artificial diffusion across the gas-liquid interface. The initially prescribed value $C_{salt}^{\Theta}(t_{init}^{\Theta}) = 0.43$ remains conserved in the liquid phase throughout the entire simulation, confirming the numerical consistency of the new advection procedure for C_{salt}^{Θ} . This phase-restricted scalar transport approach enables accurate and physically consistent analysis of the onset and transport dynamics of liquid supersaturation in evaporating falling films. Figure

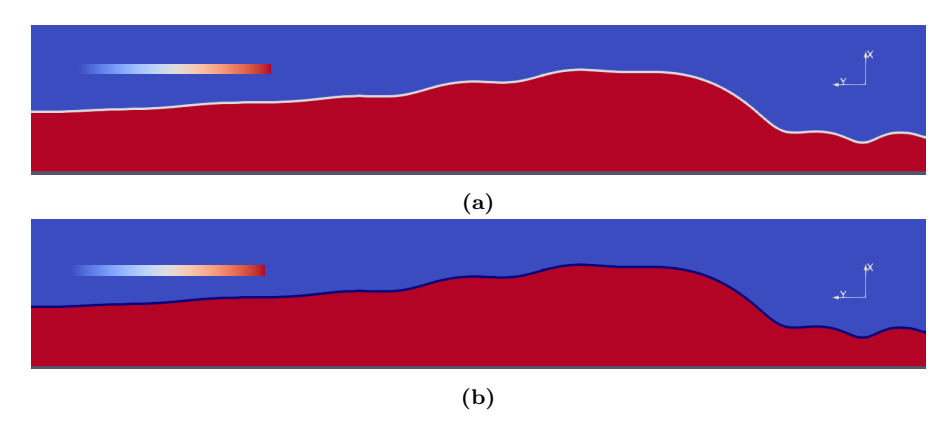


Figure 3.2: (a) Advection of the liquid volume fraction field f and (b) the salt concentration field C_{salt}^{Θ} . Flow conditions are defined by a Reynolds number Re=200 and a Kapitza number Ka=500. An initial concentration of $C_{salt}^{\Theta}(t_{init}^{\Theta})=0.43$ is prescribed in the liquid phase. The salt concentration field is now strictly confined to the liquid phase, showing no artificial diffusion across the gas-liquid interface and full conservation of C_{salt}^{Θ} during advection in the liquid phase. Both subfigures are rotated 90° counterclockwise for clarity; the white line in (a) and the black line in (b) indicate the gas-liquid interface.

(3.3) presents a quantitative comparison of the two advection schemes shown in Figure (3.1)(b) and Figure (3.2)(b). The evolution of the averaged salt concentration in the liquid is computed as

$$\langle C_{salt}^{\Theta}(t^{\Theta}) \rangle = \frac{1}{\int_{\Omega^{\Theta}} f(t^{\Theta}) d\Omega^{\Theta}} \int_{\Omega^{\Theta}} C_{salt}^{\Theta}(t^{\Theta}) f(t^{\Theta}) d\Omega^{\Theta}, \tag{3.3}$$

where the numerator represents the total salt mass within the liquid phase at time t^{Θ} and the denominator the corresponding total liquid volume in the entire computational domain Ω^{Θ} at time t^{Θ} . The results clearly demonstrate the superior mass conservation of the improved geometric advection scheme. The blue curve (corresponding to Figure 3.2(b)) maintains a constant average concentration throughout the simulation, confirming strict conservation of salt mass in the liquid phase as predicted by Eq. (3.1). In contrast, the orange curve (corresponding to Figure 3.1(b)) exhibits a steady decline in C_{salt}^{Θ} , indicating loss of salt mass caused by numerical diffusion across the gas–liquid interface when using a standard second-order advection scheme.

3.2 Scalar diffusion from interfacial cells

This section addresses the numerical treatment of scalar diffusion from the interfacial region, where the salt concentration C_{salt}^{Θ} is confined exclusively to the liquid phase. Particular emphasis is placed on the discretization of diffusion processes occurring in cells intersected by the gas-liquid interface. As outlined in 3.1, the scalar field C_{salt}^{Θ} is initialized solely within the liquid phase with an initial value of $C_{salt}^{\Theta}(t_{init}^{\Theta}) = 0.43$. The focus here lies on the subsequent diffusive transport of C_{salt}^{Θ} and is mathematical described by

$$\frac{\partial C_{salt}^{\Theta}}{\partial t^{\Theta}} = \nabla^{\Theta} \cdot \left(D_{mass}^{\Theta} \nabla^{\Theta} C_{salt}^{\Theta} \right), \tag{3.4}$$

where no source term $(S_{mass}^{\Theta} = 0)$ is included. The non-dimensional mass diffusion coefficient D_{mass}^{Θ} is defined based on scaling with the viscous length scale of the liquid film. It is therefore expressed as $D_{mass}^{\Theta} = 1/Sc$ where Sc denotes the Schmidt number, representing the ratio of momentum diffusivity to mass diffusivity. At gas-liquid interface cells, D_{mass}^{Θ} exhibits a discontinuity due to the abrupt change in fluid properties the two phases. Specifically, within the liquid phase one has $D_{mass,liq}^{\Theta} = 1/Sc_{liq}$, whereas in

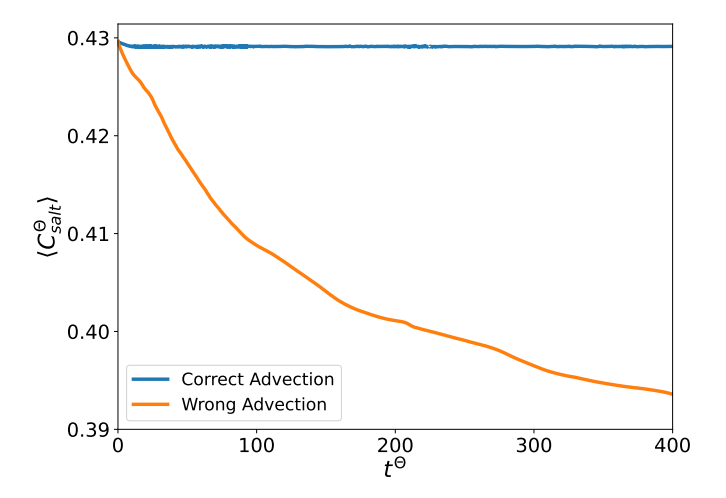


Figure 3.3: Evolution of the averaged salt concentration in the liquid $\langle C_{salt}^{\Theta} \rangle$ over time t^{Θ} . The blue curve represents the geometric advection of C_{salt}^{Θ} , while the orange curve uses a standard second-order upwind scheme. The geometric method conserves salt mass in the liquid phase, whereas the upwind scheme exhibits noticeable mass loss over time.

the gas phase the value changes sharply to $D_{mass,gas}^{\Theta} = 1/Sc_{gas}$ and typically $Sc_{liq} \neq Sc_{gas}$. When a geometric VOF interface-capturing method is employed, this discontinuity occurs over the span of a single computational cell. A common strategy to mitigate the sharp discontinuity of the mass diffusion coefficient across the gas-liquid interface is to smooth D_{mass}^{Θ} over several computational cells. This is typically achieved by applying a arithmetic mean or harmonic interpolation between the liquid and gas phase diffusion coefficients, $D_{mass,liq}^{\Theta}$ and $D_{mass,gas}^{\Theta}$, respectively [21], [22]. In non-dimensional form, the harmonic interpolation can be expressed as

$$D_{mass}^{\Theta} = \frac{1}{f \, Sc_{liq} + (1 - f) \, Sc_{qas}}.$$
 (3.5)

This smoothing approach effectively ensures a gradual transition of the diffusion coefficient when interfacial mass transfer is actually present, thereby preventing numerical oscillations at the interface. However, this approach becomes unsuitable when the scalar field is intended to remain confined to a single phase. In such cases, even though the harmonic interpolation smooths the diffusion coefficient, the sharp concentration gradient between the liquid (where $C_{salt}^{\Theta} > 0$) and the gas phase (where $C_{salt}^{\Theta} = 0$) induces a non-zero diffusive flux across the interface. As a result, artificial mass transfer occurs from the liquid into the gas phase, leading to an nonphysical leakage of the scalar field.

To illustrate the behavior of the diffusion model, a simplified test case is considered. A flat liquid film is defined, such that no wave development occurs during the simulation. The initial scalar field is prescribed as $C_{salt}^{\Theta}(t_{init}^{\Theta}) = 0.43$ within the liquid phase, while the gas phase is initialized with $C_{salt}^{\Theta}(t_{init}^{\Theta}) = 0$. The non-dimensional mass diffusion coefficients in both phases are set equal, i.e., $Sc_{liq} = Sc_{gas} = 1$. Figure (3.4) illustrates the effect of applying the harmonic mean formulation for the mass diffusion coefficient in a case where the scalar C_{salt}^{Θ} is intended to remain confined to the liquid phase. Subfigure (a) shows the initial condition at $t^{\Theta} = t_{init}^{\Theta} = 0$, where the salt concentration is present exclusively in the liquid phase and zero in the gas phase. In contrast, Subfigure (b) depicts the salt concentration field at a later time, $t^{\Theta} > 0$. It is evident that C_{salt}^{Θ} has diffused across the gas-liquid interface into the gas phase, despite the absence of any intended mass transfer. The black line in both subfigures indicates the position of the flat gas-liquid interface.

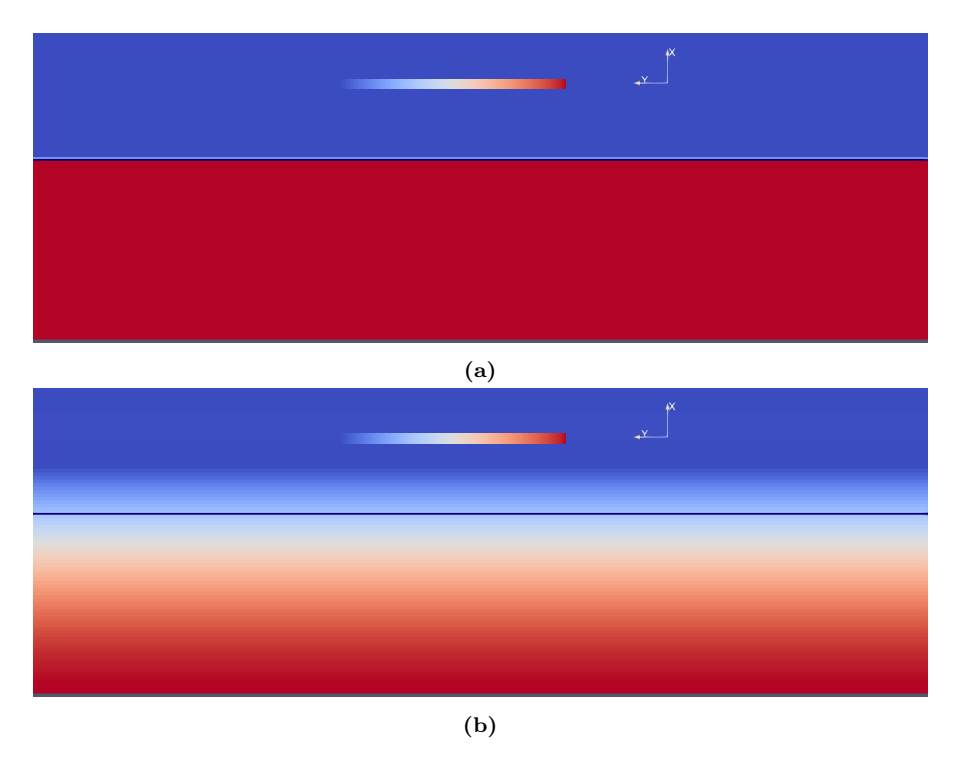


Figure 3.4: Diffusion of a scalar field confined to the liquid phase using the harmonic mean for the diffusion coefficient. (a) Initial salt concentration field, $C_{salt}^{\Theta}(t_{init}^{\Theta}) = 0.43$, in a flat falling film with Re = 200 and Ka = 500. (b) Distribution of C_{salt}^{Θ} for $t^{\Theta} > 0$. The black line denotes the gas-liquid interface, and the figure is rotated 90° counterclockwise. Diffusion of C_{salt}^{Θ} across the interface into the gas phase is clearly visible at $t^{\Theta} > 0$.

The undesired diffusion of the salt concentration into the gas phase can be prevented by enforcing an impermeable gas-liquid interface, even then when $Sc_{liq} = Sc_{gas}$. To achieve this, the first step of the PLIC method introduced in 3.1 is revisited and employed here. In this step, the interface within each interfacial computational cell is analytically reconstructed from the local volume fraction field. Based on this reconstructed interface geometry, a weighting approach is introduced to locally modify the mass diffusion coefficient at interfacial face cells. The non-dimensional mass diffusion coefficient is defined

as

$$D_{mass}^{\Theta} = D_{mass,eff}^{\Theta} \, \varphi^f, \tag{3.6}$$

where $D_{mass,eff}^{\Theta}$ represents an effective diffusion coefficient, which can be, for example, the harmonic mean or simple arithmetic average of the liquid and gas phase diffusion coefficients. The weighting factor φ^f corresponds to the fraction of liquid evaluated at the cell face, i.e., at the location where the analytically reconstructed interface intersects the computational cell surface. φ^f is obtained from the PLIC reconstruction and represents the liquid fraction at a given cell face. Within a two-dimensional square computational cell, the reconstructed interface is a straight line that can intersect any two faces of the cell, depending on the local orientation of the interface normal. Consequently, only the intersected faces exhibit partial liquid coverage, characterized by $0 < \varphi^f < 1$, while the remaining two faces are fully immersed in one or both phases — either both within the liquid phase ($\varphi^f = 1$), both within the gas phase ($\varphi^f = 0$), or one in each phase — depending on the local orientation and position of the reconstructed interface. This geometric property directly governs the diffusive transport across interfacial cells. Faces entirely located in the gas phase ($\varphi^f = 0$) contribute no diffusive flux, since the corresponding local mass diffusivity becomes zero. In contrast, faces partially or fully covered by liquid ($\varphi^f > 0$) permit diffusion in proportion to their liquid coverage, consistent with the analytically reconstructed interface geometry. Consequently, the geometrically weighted formulation of D_{mass}^{Θ} effectively enforces an impermeable gas-liquid interface and prevents non-physical scalar diffusion across it, ensuring that scalar quantities confined to one phase, such as C_{salt}^{Θ} , remain strictly within the liquid region. Further details on the numerical implementation and additional theoretical background of this weighting scheme can be found in Paper A, as well as in [8] and [20], where the treatment of diffusion from interfacial cells for scalar fields confined to a single phase is discussed in greater detail.

As a result, the aforementioned issue of nonphysical diffusion into the gas phase is resolved by applying the weighting approach, in which the effective mass diffusion coefficient is scaled by the local volume fraction value at the cell face. In addition to this special treatment of interfacial diffusion based on the analytically reconstructed interface obtained from the PLIC method, a phase-averaging approach has been implemented for the diffusion of scalar fields when the gas-liquid interface is prescribed as impermeable. This additional

treatment ensures consistency between advection and diffusion processes for scalar quantities that exhibit discontinuities across the gas–liquid interface, such as the salt concentration field C_{salt}^{Θ} . In the numerical formulation, two representations of the scalar field within interfacial cells can be distinguished: the *volume-averaged* and the *phase-averaged* formulations. The total volume of an interfacial computational cell is composed of the liquid and gas phase volumes, corresponding to their respective volume fractions. If C_{salt}^{Θ} is defined over this total cell volume, it represents a volume-averaged quantity. Since the volume fraction of the liquid phase is always known from Eq. (2.4), C_{salt}^{Θ} can alternatively be expressed only over the liquid volume within the cell, yielding a phase-averaged quantity. This distinction allows accurate representation of the scalar field in cells intersected by the interface, while maintaining strict confinement of C_{salt}^{Θ} to the liquid phase. Mathematically this two different formulations can be expressed as

$$\langle C_{salt}^{\Theta} \rangle_{V_{cell}^{\Theta}} = \frac{1}{V_{cell}^{\Theta}} \int_{V_{lin}^{\Theta}} C_{salt}^{\Theta} dV^{\Theta} = \frac{V_{liq}^{\Theta}}{V_{cell}^{\Theta}} C_{salt}^{\Theta} = f C_{salt}^{\Theta}, \tag{3.7}$$

$$\langle C_{salt}^{\Theta} \rangle_{V_{liq}^{\Theta}} = \frac{1}{V_{liq}^{\Theta}} \int_{V_{liq}^{\Theta}} C_{salt}^{\Theta} dV^{\Theta} = \frac{1}{V_{liq}^{\Theta}} C_{salt}^{\Theta} V_{liq}^{\Theta} = C_{salt}^{\Theta}, \qquad (3.8)$$

where $\langle C_{salt}^{\Theta} \rangle_{V_{cell}^{\Theta}}$ is the volume-averaged salt concentration field, $\langle C_{salt}^{\Theta} \rangle_{V_{liq}^{\Theta}}$ the liquid-phase averaged salt concentration field, V_{cell}^{Θ} and, V_{liq}^{Θ} the total cell volume and the liquid phase cell volume in a computational cell, respectively. The relationship between volume- and phase-average is given by

$$\langle C_{salt}^{\Theta} \rangle_{V_{liq}^{\Theta}} = \frac{\langle C_{salt}^{\Theta} \rangle_{V_{cell}^{\Theta}}}{f} = \frac{C_{salt}^{\Theta}}{f} = \langle C_{salt}^{\Theta} \rangle_{liq}, \tag{3.9}$$

where the volume-averaged salt concentration field is already by definition C_{salt}^{Θ} . The distinction between volume- and phase-averaged quantities becomes particularly important in interfacial cells, where 0 < f < 1. In such cells, a total volume average would artificially dilute the concentration field and consequently underestimate the diffusive flux into neighboring pure-phase cells. Therefore, in addition to the modification of the mass diffusion coefficient described earlier, the diffusion equation Eq. (3.4) is solved for the phase-averaged scalar quantity according to Eq. (3.9). This formulation ensures that scalar gradients are correctly evaluated and that the diffusive fluxes

from interfacial cells into pure-phase regions — such as the liquid phase in the present case — are physically consistent. After completing the diffusion step for the phase-averaged salt concentration field, a back-transformation to the corresponding volume-averaged field is performed. The exact same methodology is also applicable when evaporation is present at interfacial cells and therefore $S_{mass}^{\Theta} \neq 0$. This procedure guarantees consistency with the advection step of C_{salt}^{Θ} , which employs geometrically computed fluxes based on the VOF interface reconstruction, where the volume-averaged scalar quantity is considered [8], [23].

Figure (3.5)(a) presents the results for the same simulation setup as in Figure (3.4), but with the weighting method based on the analytically reconstructed interface used to modify D_{mass}^{Θ} . A comparison between Figure (3.5)(a) and Figure (3.4)(b), both corresponding to $t^{\Theta} > 0$, reveals a significant improvement. When the weighted formulation of D_{mass}^{Θ} is employed instead of the simple harmonic mean, the scalar field C_{salt}^{Θ} remains fully confined to the liquid phase, with no artificial diffusion into the gas phase. This demonstrates the effectiveness of the geometrically based weighting scheme in enforcing an impermeable interface for scalar quantities confined to a single phase, such as C_{salt}^{Θ} . In addition to the treatment of the mass diffusivity, Figure (3.5)(b) illustrates the behavior of C_{salt}^{Θ} in the interfacial cells when the phase-averaged formulation is applied. The white line indicates the gas-liquid interface, where the scalar field C_{salt}^{Θ} remains sharp and exhibits a discontinuous transition into the gas phase. The phase-averaged method, used in combination with the geometrically weighted formulation of D_{mass}^{Θ} , therefore provides a physically consistent and robust numerical approach for cases in which a scalar field is confined to a single phase and no mass transfer across the interface is permitted.

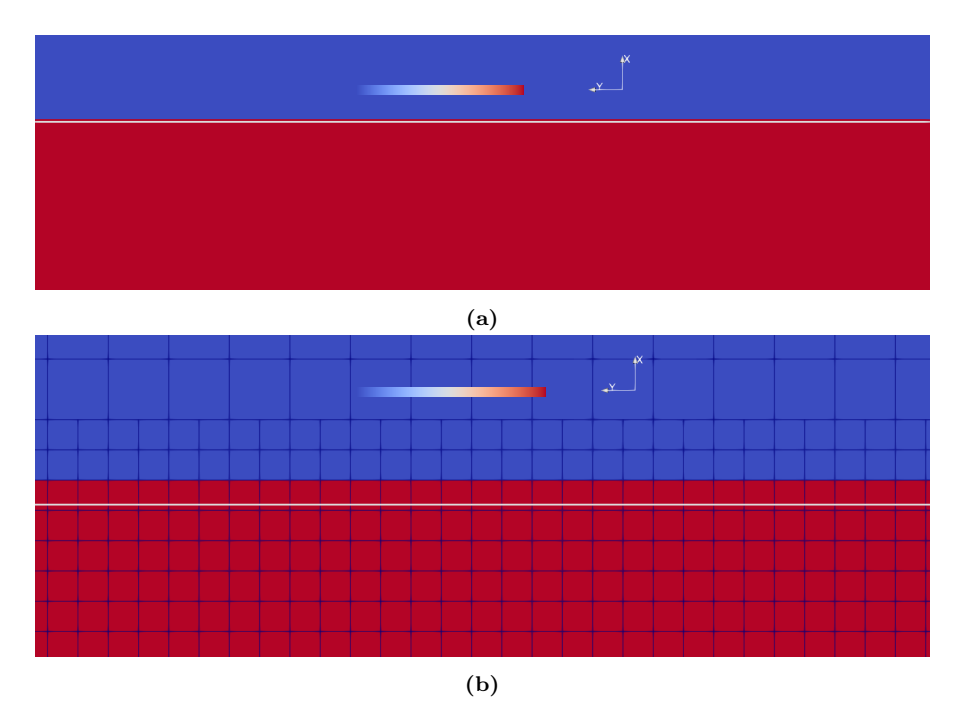


Figure 3.5: Diffusion of a scalar field confined to one phase using the geometric weighting method for the mass diffusivity combined with a phase-averaged scalar formulation. (a) Distribution of C_{salt}^{Θ} for $t^{\Theta} > 0$ in a flat falling film with Re = 200 and Ka = 500. (b) Phase-averaged treatment of scalar field in interfacial cells. The white line denotes the gas-liquid interface, and the figure is rotated 90° counterclockwise. The scalar field remains confined to the liquid phase and preserves a sharp discontinuity across the interface, in contrast to Figure (3.4) (b). The phase-averaged salt concentration expression, $\langle C_{salt}^{\Theta} \rangle_{liq}$, is shown.

An additional demonstration of the robustness of this combined approach is shown in Figure (3.6), which presents a result from $Paper\ A$ and [8]. In this case, a localized source term is introduced within the interfacial cells, and diffusion occurs exclusively into the liquid phase while the phase-averaged scalar formulation is employed during the diffusion step. This further highlights the accuracy and physical consistency of the method in handling scalar transport confined to a single phase.

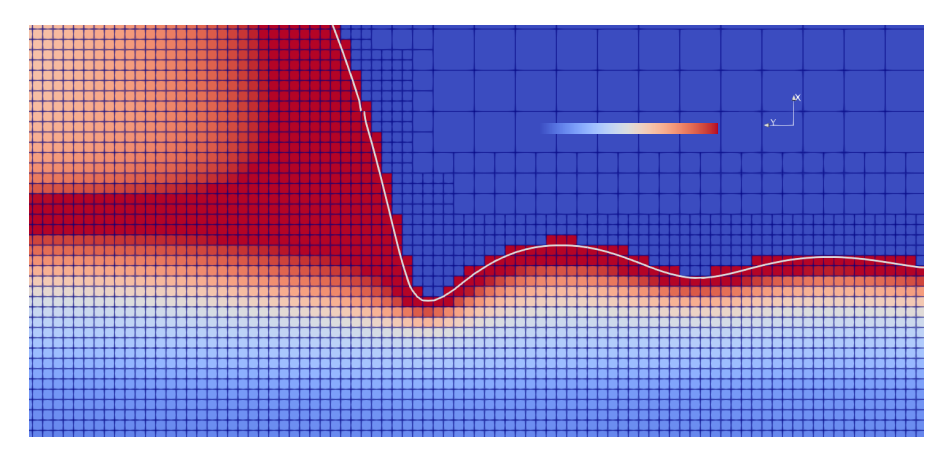


Figure 3.6: Zoomed-in view of the non-dimensional, liquid-phase-averaged salt concentration field, $\langle C_{salt}^{\Theta} \rangle_{liq}$ (see Eq. 3.9), in the capillary region upstream of the solitary wave for Re=200 and Ka=500. The overlaid computational grid and the white contour marking the gas-liquid interface highlight the fine spatial resolution of interfacial curvature and the steep mass-transfer boundary layer. The liquid-phase averaging treats C_{salt}^{Θ} as discontinuous across interfacial cells, while the geometrical weighting ensures diffusion occurs strictly into liquid-phase cells, preventing any artificial transport into the gas phase.

Finally, the same quantitative analysis described in 3.1 is performed here, with the results presented in Figure (3.7). The orange curve depicts the temporal evolution of the average salt concentration within the liquid phase when using the harmonic mean for the mass diffusion coefficient, while the blue curve corresponds to the case employing the geometrically weighted formulation of D_{mass}^{Θ} . It is evident that the geometrically weighted approach (blue curve) conserves the total salt mass within the liquid phase throughout the simulation, whereas the harmonic mean formulation (orange curve) leads to an artificial mass loss into the gas phase due to nonphysical diffusion across the interface.

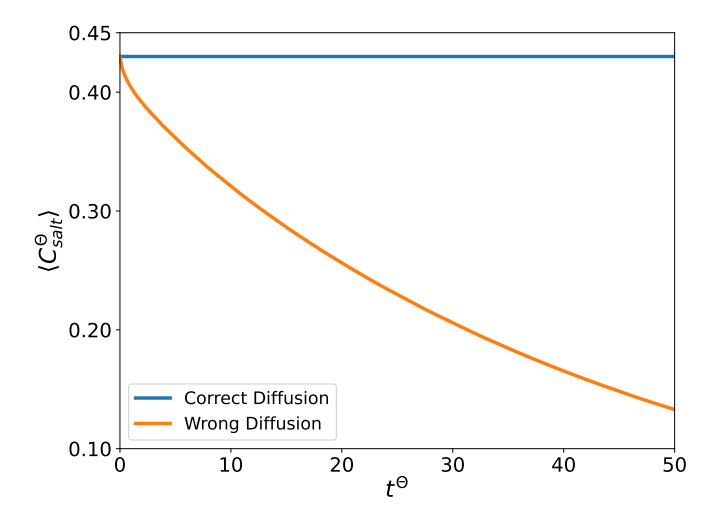


Figure 3.7: Temporal evolution of the average salt concentration in the liquid phase. The blue curve corresponds to the geometric weighting method for the mass diffusion coefficient combined with the phase-averaged scalar formulation, while the orange curve represents the harmonic-mean approach. The harmonic-mean case shows an artificial loss of salt mass due to nonphysical diffusion across the gas—liquid interface, whereas the geometric weighting with phase averaging conserves mass in the liquid phase and maintains the scalar field confined to the liquid phase at its initial value throughout the simulation.

CHAPTER 4

Concluding Remarks and Future Work

Crystallization fouling in evaporating falling liquid films — defined as the undesired deposition of solid particles on heated surfaces and the subsequent formation of fouling layers — remains a major challenge across many industrial processes. Such deposits reduce thermal efficiency, hinder heat and mass transfer, and can ultimately lead to partial or complete shutdowns of production systems. To investigate the precursors of crystallization fouling, specifically the formation and evolution of supersaturation, a multiphase Direct Numerical Simulation (DNS) framework was developed. This framework fully resolves the hydrodynamics and interfacial dynamics of an evaporating falling film exposed to a gas phase and accurately captures the coupled heat and mass transfer phenomena that give rise to local supersaturation within the liquid. As presented in [8], the simulations reveal that supersaturation develops initially near the gas-liquid interface as a result of interfacial evaporation, where the removal of water locally increases the salt concentration. These highly supersaturated regions are subsequently transported into the bulk liquid by diffusion, advection, and recirculation within the film, leading to a broader spatial distribution of supersaturation. The study further shows that higher wetting rates (increased Reynolds numbers) enhance mixing and promote a more uniform distribution of supersaturation, whereas at low wetting rates, supersaturated regions remain localized within specific zones of the film.

During the development of the DNS framework, several numerical challenges were encountered, as discussed in 3. Since supersaturation occurs exclusively within the liquid phase, scalar quantities such as temperature and salt concentration must likewise remain confined to the liquid domain. While this condition is physically intuitive — because, in the absence of mass transfer across the gas-liquid interface, the salt should remain entirely within the liquid — it poses a significant numerical challenge. As demonstrated in 3.1 and 3.2, without dedicated numerical treatment of the advection and diffusion processes, artificial mass diffusion can occur, leading to a nonphysical leakage of the scalar field across the gas-liquid interface into the gas phase. Such behavior violates mass conservation within the liquid phase and results in erroneous supersaturation fields. By addressing this issue through specialized interfacial treatments for scalar transport, the present framework ensures strict confinement of the salt concentration to the liquid phase, thereby enabling accurate tracking and analysis of supersaturation dynamics under various hydrodynamic conditions in evaporating falling films.

As part of the ongoing research, the Eulerian multiphase DNS framework is being extended through coupling with a Lagrangian point-particle approach. This development enables the simultaneous investigation of liquid-phase supersaturation and the dynamics of nucleated particles in vertical falling films. In the initial stage, spherical particles of constant size are considered to study their transport from the supersaturated regions near the gas-liquid interface into the bulk liquid and towards the solid wall. Particular emphasis is placed on the near-wall particle behavior, where hydrodynamic interactions and wallbounded effects strongly influence lateral motion and deposition. This aspect is critical for understanding crystallization fouling, particle adhesion, and the subsequent formation of solid fouling layers. Following this stage, the framework will be further advanced to include fully coupled particle-solute interactions, where individual particles respond to but also influence the evolving salt concentration field. This will allow for direct simulation of crystal growth driven by local supersaturation and the detailed study of transport and deposition mechanisms at the heated solid boundary.

References

- [1] A. Åkesjö, "Hydrodynamics and heat transfer in vertical falling films with smooth and modified heat-transfer surfaces an experimental and numerical investigation," Ph.D. dissertation, Chalmers University of Technology, 2018.
- [2] S. Kalliadasis, C. Ruyer-Quil, B. Scheid, and M. Velarde, *Falling Liquid Films*. Applied Mathematical Sciences, Springer, 2012.
- [3] M. Gourdon, D. Strömblad, L. Olausson, and L. Vamling, "Scale formation and growth when evaporating black liquor with high carbonate to sulphate ratio," Nordic Pulp and Paper Research Journal, vol. 23, 2008.
- [4] J. Darand and A. Jafarian, "Long-term simulation of crystallization fouling in a forced circulation crystallizer," *International Journal of Heat and Mass Transfer*, vol. 231, 2024.
- [5] A. Mersmann, Crystallization Technology Handbook. Marcel Dekker, Inc., 2001.
- [6] B. Shi, "Crystallization of solutes that lead to scale formation in black liquor evaporation," Ph.D. dissertation, Georgia Institute of Technology, 2002.
- [7] J. Berce, M. Zupancic, M. Moze, and I. Golobic, "A review of crystal-lization fouling in heat exchangers," *Processes 9 (8)*, 2021.

- [8] D. Vleeschhouwers, N. Hidman, A. Åkesjö, H. Ström, and S. Sasic, "Liquid supersaturation in evaporating vertical falling films a direct numerical simulation study," *International Journal of Heat and Mass Transfer*, vol. 255, p. 127760, 2026.
- [9] G. Schnabel, M3 Heat Transfer to Falling Films at Vertical Surfaces.
 VDI Heat Atlas, Springer, 2010.
- [10] S. Popinet, "Gerris: A tree-based adaptive solver for the incompressible euler equations in complex geometries," *Journal of Computational Physics*, vol. 190, pp. 572–600, 2003.
- [11] S. Popinet, "An accurate adaptive solver for surface-tension-driven interfacial flows," *Journal of Computational Physics*, vol. 228, pp. 5838–5866, 2009.
- [12] S. Popinet, "A quadtree-adaptive multigrid solver for the serre-green-naghdi equations," *Journal of Computational Physics*, vol. 302, pp. 336–358, 2015.
- [13] G. Dietze, "Effect of wall corrugations on scalar transfer to a wavy falling liquid film," *Journal of Fluid Mechanics*, vol. 859, pp. 1098–1128, 2019.
- [14] P. Farsoiya, S. Popinet, and L. Deike, "Bubble-mediated transfer of dilute gas in turbulence," *Journal of Fluid Mechanics*, vol. 920, A34 1–21, 2021.
- [15] N. Hidman et al., "How surface modifications enhance vertical falling film evaporation," *Journal of Fluid Mechanics*, vol. 997, pp. 17–32, 2024.
- [16] P. Saffman, "The lift on a small sphere in a slow shear flow," *Journal of Fluid Mechanics*, vol. 22 (2), pp. 385–400, 1965.
- [17] M. Maxey and J. Riley, "Equation of motion for a small rigid sphere in a nonuniform flow," *Physics of Fluids*, vol. 26, pp. 883–889, 1983.
- [18] R. Scardovelli and S. Zaleski, "Direct numerical simulation of free-surface and interfacial flows," *Annn. Rev. Fluid Mechanics*, vol. 31, pp. 567–603, 1999.
- [19] D. Bothe and S. Fleckenstein, "A volume-of-fluid-based method for mass transfer processes at fluid particles," *Chemical Engineering Science*, vol. 101, pp. 283–302, 2013.

- [20] J. Lopez-Herrera, A. Ganan-Calvo, S. Popinet, and M. Herrada, "Electrokinetic effects in the breakup of electrified jets: A volume-of-fluid numerical study," *International Journal of Multiphase Flow*, vol. 71, pp. 14–22, 2015.
- [21] Y. Haroun, D. Legendre, and L. Raynal, "Direct numerical simulation of reactive absorption in gas-liquid flow on structured packing using interface capturing method," *Chemical Engineering Science*, vol. 65, pp. 351– 356, 2010.
- [22] J. Maes and C. Soulaine, "A new compressive scheme to simulate species transfer across fluid interfaces using the volume-of-fluid method," *Chemical Engineering Science*, vol. 190, pp. 405–418, 2018.
- [23] A. Tourbier, L. Gamet, P. Beard, T. Michel, J. Aubin, and H. Jasak, "A consistent methodology to transport a passive scalar with the geometric volume-of-fluid method isoadvector," *Journal of Computational Physics*, vol. 513, p. 113 198, 2024.

Part II

Papers



Liquid supersaturation in evaporating vertical falling films - A direct numerical simulation study

Denis Vleeschhouwers, Niklas Hidman, Anders Åkesjö, Henrik Ström, Srdjan Sasic

Published in International Journal of Heat and Mass Transfer, vol. 255, pp. 127760, (2026). https://doi.org/10.1016/j.ijheatmasstransfer.2025.127760.



Inertial particle dynamics in vertical wavy falling films

Denis Vleeschhouwers, Niklas Hidman, Anders Åkesjö, Henrik Ström, Srdjan Sasic

To be submitted to a scientific journal (2026).